Journal of Geophysical Research: Earth Surface

RESEARCH ARTICLE
10.1029/2017JF004520

Glacier Calving Rates Due to Subglacial Discharge, Fjord Circulation, and Free Convection

K. M. Schild[1,2], C. E. Renshaw[1], D. I. Benn[3], A. Luckman[4,5], R. L. Hawley[1], P. How[6,7], L. Trusel[8], F. R. Cottier[9,10], A. Pramanik[11], and N. R. J. Hulton[7]

[1]Department of Earth Sciences, Dartmouth College, Hanover, NH, USA, [2]Department of Earth Sciences, Now at University of Oregon, Eugene, OR, USA, [3]School of Geography and Geosciences, University of St Andrews, Saint Andrews, UK, [4]Department of Geography, Swansea University, Swansea, UK, [5]Arctic Geophysics, University Centre in Svalbard, Longyearbyen, Svalbard, [6]School of GeoSciences, University of Edinburgh, Edinburgh, UK, [7]Arctic Geology, University Centre in Svalbard, Longyearbyen, Svalbard, [8]Department of Geology, Rowan University, Glassboro, NJ, USA, [9]Scottish Association for Marine Science, Oban, UK, [10]Department of Arctic and Marine Biology, UiT The Arctic University of Norway, Tromsø, Norway, [11]Department of Geology and Geophysics, Norwegian Polar Institute, Tromsø, Norway

Key Points:
- We partition calving rate due to submarine melt into calving due to free convection, horizontal fjord circulation, and meltwater discharge
- The calving rate due to meltwater discharge is up to an order of magnitude larger than fjord circulation and free convection calving rates
- A given flux of meltwater has a greater impact on calving rate at the end of the melt season than in the early melt season

Correspondence to:
K. M. Schild,
schild.km@gmail.com

Citation:
Schild, K. M., Renshaw, C. E., Benn, D. I., Luckman, A., Hawley, R. L., How, P., et al. (2018). Glacier calving rates due to subglacial discharge, fjord circulation, and free convection. *Journal of Geophysical Research: Earth Surface*, *123*. https://doi.org/10.1029/2017JF004520

Received 12 OCT 2017
Accepted 2 AUG 2018
Accepted article online 22 AUG 2018

Abstract Tidewater glacier calving provides the most direct mechanism of ice transfer from land to the ocean. However, the physical melt processes influencing calving remain challenging to constrain. In this study we focus on calving rates at Kongsbreen, a tidewater glacier in Svalbard, due to three mechanisms of submarine melt: (1) free convection, (2) horizontal fjord circulation, and (3) meltwater discharge. To calculate an overall calving rate, we measure glacier velocity and terminus change using Sentinel imagery. We calculate free convection, fjord circulation, and meltwater discharge calving using mooring data for mid-fjord ocean temperature (30–80 m depth), reanalysis results for meltwater runoff, and georectified time-lapse imagery to track icebergs and infer surface circulation. Results show that the total glacier calving rate is highly correlated with ocean temperature during the 2016 melt season. When runoff was present, we found that subglacial discharge accounted for calving rates an order of magnitude greater than the maximum calving rates assigned to the other two melting mechanisms combined. Further, subglacial discharge at Kongsbreen was more efficient in inducing calving later in the season than earlier in the season, implying that the increase in ocean temperatures, the timing of meltwater discharge within a melt season, and/or the development of discrete meltwater exit channels are critical components to calving rates. As the recent atmospheric warming trend and subsequent increase in meltwater discharge is expected to continue, it is essential to understand the processes contributing to an increase in glacier calving and incorporate these processes into predictive models.

1. Introduction

Tidewater glaciers transport mass directly from land to the ocean through frontal ablation: the combined result of iceberg calving and submarine melting of the terminus face. Since mass loss from these glaciers has an immediate impact on sea level, understanding the processes central to the rate of tidewater glacier frontal ablation is critical to accurately predicting the cryospheric contribution to global sea level rise in a warming climate. The recent coincident timing of Arctic tidewater glacier acceleration, increased calving, and atmospheric and oceanic warming suggests that one or more processes acting at the ice-ocean boundary may be a controlling mechanism on tidewater glacier frontal ablation, particularly those relating to ocean temperature (Holland et al., 2008; Howat et al., 2007; Luckman et al., 2015; Nick et al., 2009; Straneo & Heimbach, 2013; van den Broeke et al., 2009) and to the development of subglacial meltwater channels (Slater et al., 2016). Submarine melting, specifically melt undercutting, often facilitates calving (e.g., Benn et al., 2017; O'Leary & Christoffersen, 2013; Slater et al., 2017), and therefore quantifying submarine melt processes is central to understanding the mechanisms operating at the ice-ocean interface. However, progress towards understanding and quantifying the controls on frontal ablation has been hindered by the challenges associated with collecting in situ measurements in this environment. Most notably, processes linking melt to calving have rarely been quantified. Here we propose a new partitioning of the total glacier calving rate into the calving rates due to three simplified mechanisms of submarine melt, and apply this partitioning at a Svalbard tidewater glacier. In attributing calving rates to specific processes at the ice-ocean interface, our results allow for more accurate characterization and prediction of glacier behavior.

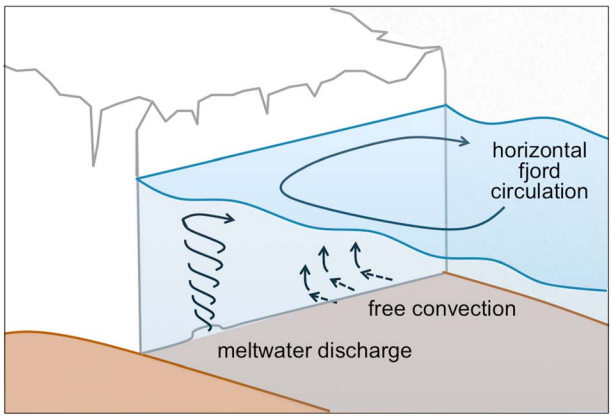

Figure 1. Three broad mechanisms of submarine melting as they are partitioned in this study. Melting mechanisms include: (1) free convection, (2) horizontal fjord circulation, and (3) meltwater discharge. Arrows indicate possible directions of water movement.

2. Background

Tidewater glacier calving style and calving rate are influenced by several environmental factors, including glacier and fjord geometry (Enderlin et al., 2013; Schild & Hamilton, 2013), the presence or strength of a buttressing mélange (Amundson et al., 2010; Christoffersen et al., 2012; Vieli & Nick, 2011), the bathymetry of the fjord (Nick et al., 2013; Rignot et al., 2016), and ocean temperature and circulation (Holland et al., 2008; Luckman et al., 2015; Straneo & Heimbach, 2013). Calving style (e.g., tabular, flakes, and rotating icebergs) is largely controlled by internal glacier processes, including glacier velocity and strain rates (Bassis & Jacobs, 2013; Benn et al., 2007), with individual calving events influenced by processes at the ice-ocean interface, including crevasse fracture propagation, submarine melting, and glacier bending at the grounding line (Benn et al., 2007, 2017). Recent modeling studies have pointed to two distinct calving styles resulting from melt undercut: small calving events only impacting ice directly above the melt undercut region (no amplification; Benn et al., 2017) and large calving events incorporating ice beyond the melt undercut region (with amplification). The second scenario includes the melting of larger portions of the supporting ice below the waterline, creating ice weaknesses, which propagate upglacier and intensify calving (Benn et al., 2017; O'Leary & Christoffersen, 2013). Based upon these two different scenarios, the calving rate due to submarine melting would be dependent upon the degree of submarine melting prior to a calving event. Recent studies in Svalbard have shown that submarine melting, specifically small-scale melt undercut, is likely a dominant driver of calving at grounded Svalbard tidewater glaciers (Benn et al., 2017; How et al., 2017) and that the overall calving rate is highly correlated with the ocean temperature (Luckman et al., 2015).

Oceanographic studies estimating submarine melt rates have used field measurements of conductivity, temperature, and depth (CTD) collected from boats, helicopters, or moorings to quantify up-fjord heat transport. Ship and helicopter-based CTD casts (e.g., Cottier et al., 2005; Holland et al., 2008; Straneo et al., 2010; Sutherland & Straneo, 2012) serve as point measurements, but are seasonally biased, as the location of the CTD cast and the timing of these deployments are dictated by variables such as mélange and sea ice cover, thereby limiting studies to predominantly summer months (May–September). Additionally, the seasonal or long-term melt rates are harder to extrapolate from point measurements alone, as these measurements represent a temporal snapshot of a dynamic system (e.g., Jackson et al., 2014; Jackson & Straneo, 2016; Straneo et al., 2010). Instrumented remotely operated vehicles (ROVs) and autonomous underwater vehicles (AUVs) have successfully measured temperature and salinity close to an actively calving terminus (e.g., Mankoff et al., 2016; Stevens et al., 2016), but require an open path for travel and are therefore susceptible to the limitations listed above. Permanent moorings can provide a full seasonal record (e.g., Cottier et al., 2005; Inall et al., 2014; Jackson et al., 2014; Luckman et al., 2015; Straneo et al., 2010), however they must be placed a safe distance away from the terminus and any passing icebergs. As such they are generally deployed down-fjord or in protected coves, well away from the calving glacier terminus. Nevertheless, successful mooring deployments and retrievals have occurred closer to the glacier terminus in fjords with smaller icebergs (e.g., Cottier et al., 2005).

The degree of submarine melt is dependent upon the temperature of the ocean water and the movement of water within the fjord. Fjord circulation is driven by local density gradients between ocean water and fresh water, as well as mechanical forcing from subglacial discharge plumes or the wind. While fjord circulation involves a series of complex relationships between the ocean water, freshwater, and the melting of ice, three broad mechanisms of submarine melting have been identified through models and field campaigns: (1) free convection (e.g., Chauché et al., 2014; El-Tahan et al., 1987; Magorrian & Wells, 2016), (2) horizontal fjord circulation (Cowton et al., 2015), and (3) meltwater discharge (e.g., Carroll et al., 2016; Cenedese & Linden, 2014; Chauché et al., 2014; Christoffersen et al., 2012; Kimura et al., 2014; Motyka et al., 2013; Slater et al., 2016; Xu et al., 2012; Figure 1).

The first mechanism of submarine melt, free convection (also referred to as melt-driven convection), occurs when ocean water comes in contact with the glacier terminus, melting the glacier ice, and

thereby introducing freshwater to the system. This freshwater initiates a density-driven circulation, or free convection, with freshwater moving buoyantly up the ice face displacing ocean water (e.g., El-Tahan et al., 1987; Josberger, 1977; Magorrian & Wells, 2016). Free convection drives only weak fjord circulation, which might easily be overwhelmed by the other two circulation processes.

In the second form of submarine melting, horizontal fjord circulation, melting occurs as ocean water is moved horizontally along the terminus. While this horizontal surface circulation may potentially have a larger impact on submarine melting than free convection due to the forced movement of water, there have been no direct measurements of this process. Preliminary model results suggest that melting due to horizontal surface fjord circulation external to a meltwater discharge plume is minimal (Cowton et al., 2015). However, the spatial resolution of the model (200 m) may be too course to sufficiently resolve near ice circulation. Additionally, this model has so far only included surface circulation as initiated by subglacial meltwater discharge, and therefore does not include other potential drivers of circulation, such as wind or tides, and consequently may underestimate the melting.

The third mechanism of submarine melt, meltwater discharge, has a dominant control on along-fjord circulation (Xu et al., 2012). As meltwater exits the subglacial environment, it begins to rise buoyantly towards the surface, entraining warm ocean water in the process. This water mixture flows vertically against the terminus until it reaches the surface or entrains enough ocean water for the density of the buoyant plume to equilibrate with the ambient fjord water, melting the terminus in the process. In systems with prominent subglacial meltwater discharge locations, this submarine melt is localized and results in melt undercutting and calving immediately above the discharge location, locally accelerating calving and generating an embayment within the ice face (Fried et al., 2015; Slater et al., 2015). However, in systems with multiple discharge locations, the number of exit points and distance between them is important to the overall impact of submarine melting. If two large plumes are close together, the plumes can coalesce (Cenedese & Linden, 2014; Kimura et al., 2014) and the overall melt decreases when compared with two independent plumes, however if the terminus is scattered with subglacial discharge locations, the combined melting of all the discharge locations can be larger than one single location (Fried et al., 2015; Slater et al., 2015).

O'Leary and Christoffersen (2013) represented the relationship between submarine melt rate and calving rate in terms of the total glacier calving rate (ice loss per time), $\dot{c}_{total}$, such that

$$\dot{c}_{total} = \dot{c_d} + \dot{c}_{sub}, \tag{1}$$

and

$$\dot{c}_{sub} = \omega \dot{m}_{sub}. \tag{2}$$

Here $\dot{c_d}$ is the dry calving rate, or the calving rate of the glacier without the influence of submarine melt, relating to ice temperature, strain rate, and predominant crevasse separation. The calving rate due to all mechanisms of submarine melt, $\dot{c}_{sub}$, is the product of the amplification factor, ω, and the terminus melt rate encompassing all mechanisms of submarine melt, $\dot{m}_{sub}$. Localized melting induces structural weakness which results in brittle failure (calving) of the glacier terminus. Thus, the total mass loss due to submarine melting may be greater than just the mass loss due to melting, and an amplification factor must be introduced. O'Leary and Christoffersen (2013) proposed that the degree of amplification ($\omega \approx 1$–6) is based upon glacier geometry, closeness to flotation, and the nature of the crevasse pattern.

In this study, we use a combination of in situ ocean temperature data and in situ and remotely sensed imagery to quantify free convection calving, develop a new methodology to quantify fjord circulation calving rates, use calving style to quantify the dry calving rate, and attribute the remainder of the total glacier calving rate to meltwater discharge calving. We demonstrate this methodology by calculating the contribution from each of the three submarine melt mechanisms over the 2016 melt season for Kongsbreen, a tidewater glacier in Svalbard.

3. Methods

3.1. Study Location

Kongsbreen (78.96°N, 12.61°E, 378 km^2) is located on the west coast of Spitsbergen, the largest island in the Svalbard archipelago and shares a fjord with the research base and town of Ny-Ålesund (Figure 2a). The Svalbard archipelago is ~60,000 km^2 and located midway between mainland Norway and the North Pole. We choose Kongsbreen for this study largely due to its accessibility, mélange-free terminus during the summer months, availability of time-lapse camera and satellite imagery, and richness of in situ measurements. The overlap of these remote sensing and in situ measurements defines the study period as 10 April to 7 October (day 101–281) 2016. Kongsbreen has a nunatak dividing the terminus into two branches (Figure 2a), the northern branch (Figure 2b) drains into Kongsfjorden, which is ~140 m deep at the terminus (2007 position; Schellenberger et al., 2015), while the southern branch is much slower and partially land-terminating. We therefore focus our study on the northern branch, as it is also one of the fastest flowing, non-surging tidewater glaciers in Svalbard (Blaszczyk et al., 2009; Schellenberger et al., 2015). Between 1990 and 2007, the terminus of Kongsbreen's northern branch, hereafter referred to as Kongsbreen, was at a stable position. Since 2007, it has retreated and accelerated, reaching a peak flow speed of 2.7 m/day in 2013 (Schellenberger et al., 2015). Kongsbreen has one prominent subglacial discharge location across the width of its terminus (Figure 2b, red triangle), where a spatially static but variably sized sediment plume, visible at the fjord surface, is present during the summer months.

3.2. Partitioning the Calving Rate

We partition the calving rate due to submarine melt ($\dot{c}_{sub}$ in equation (1)) to quantify the individual calving rates due to free convection, fjord circulation, and meltwater discharge. Specifically, we modify equation (2) to separate calving rates into these simplified mechanisms of submarine melt and expand equation (1) to become:

$$\dot{c}_{total} = \dot{c}_d + \dot{c}_{free} + \dot{c}_{circ} + \dot{c}_{MW}, \tag{3}$$

where $\dot{c}_{free}$ is the calving rate due to free convection, $\dot{c}_{circ}$ is the calving rate due to horizontal fjord circulation, and $\dot{c}_{MW}$ is the calving rate due to meltwater discharge. These calving rates are defined as

$$\dot{c}_{free} = \omega_f \dot{m}_{free}, \tag{4}$$

$$\dot{c}_{circ} = \omega_f \dot{m}_{circ}, \tag{5}$$

and

$$\dot{c}_{MW} = \omega_{MW} \dot{m}_{MW}. \tag{6}$$

Here ω_f remains the wet calving multiplier for both the melt rate due to free convection ($\dot{m}_{free}$) and fjord circulation ($\dot{m}_{circ}$). The calving rate due to meltwater discharge ($\dot{c}_{MW}$) uses a potentially different calving multiplier, ω_{MW}. We justify the use of separate amplification factors for free convection and fjord circulation (ω_f) versus meltwater discharge (ω_{MW}) on the basis that melting due to free convection and fjord circulation act across the entire width of the terminus, while direct melting due to meltwater discharge is likely spatially localized due to the single prominent discharge location at Kongsbreen. Additionally, melting at one prominent location can result in a similarly localized stress field, and a modification of the overall terminus shape. During peak meltwater discharge, focused calving results in an indent of the terminus at the prominent discharge location. This behavior is in contrast to the more spatially uniform stress field created by melting across the entire terminus width, as with free convection and fjord circulation.

3.3. Calculating Glacier Velocity and the Total Glacier Calving Rate ($\dot{c}_{total}$)

As in Benn et al. (2007), we determine the total glacier calving rate by measuring the difference between glacier velocity (ϑ_g) at the terminus and change in glacier terminus position over a period of time ($^{dP}/_{dt}$):

$$\dot{c}_{total} = \vartheta_g - \frac{dP}{dt}. \tag{7}$$

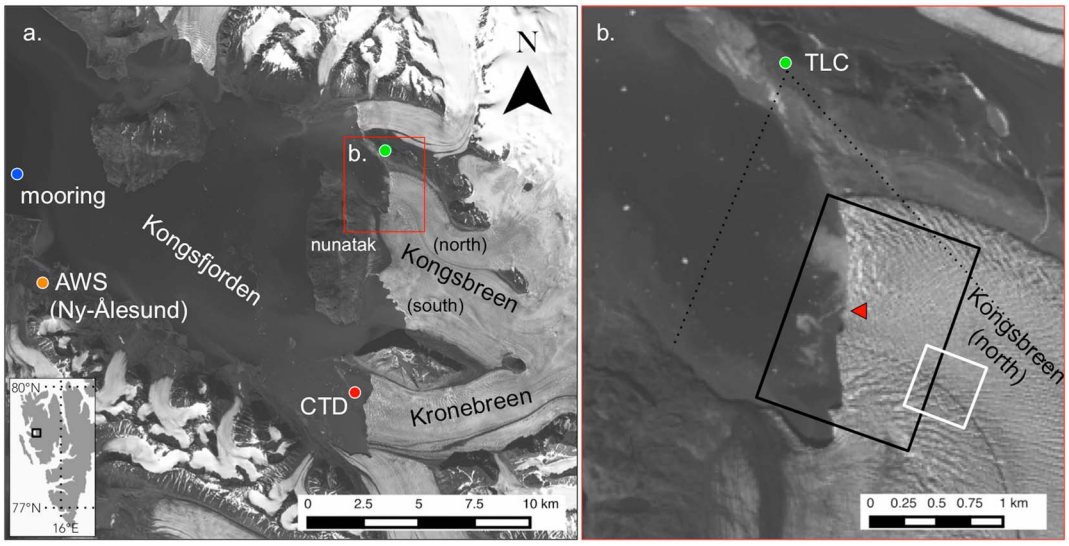

Figure 2. Location map of Kongsbreen, Svalbard (inset), showing the northern and southern branches (a) and an enlarged map of the northern branch (b). The prominent subglacial discharge location (b, red triangle) is labeled, as well as the time-lapse camera (TLC; a, b, green circle), automatic weather station (AWS; a, orange circle), mooring (a, blue circle), CTD cast (a, red circle), and areas of the glacier and fjord used to calculate iceberg velocity (b, black box), calving rate (b, black box), and glacier velocity (b, white box). Background Landsat-8 image (a, b) was collected on 2 July 2016.

We use Sentinel-1a synthetic aperture radar (SAR) imagery to measure the change in terminus position and calculate glacier velocities. Sentinel is a European Space Agency constellation composed of several satellites, with Sentinel-1a and Sentinel-1b carrying identical C-band (5.405 GHz) SAR instruments operating in four different modes. In this study, we use the interferometric wide swath (IW) mode with ~5 × 20 m (range × azimuth) spatial resolution. Sentinel-1a has a 12-day orbit and, because it is an active radar sensor, polar darkness and cloud cover do not hinder image collection. We use 11 Sentinel-1a images of Kongsbreen during the time-lapse camera image acquisition (30 April to 15 September) and an additional four images to bookend this period (two on each end).

To calculate the change in terminus position, we follow the methods of Moon and Joughin (2008), first digitizing the glacier terminus position, and then measuring the area upglacier of the terminus within a projected standardized box (Figure 2b, black box). We divide the upglacier area by the width of the standardized box (1,336 m), resulting in a normalized terminus position (*P*; as in Schild & Hamilton, 2013). Using the width-averaged method, the location of area loss, whether focused at a meltwater discharge location or spread across the width of the terminus, will be indistinguishable. Therefore, we use this method in combination with the manually digitized terminus positions to identify locations of increased calving activity throughout the melt season.

To derive glacier velocity, we apply feature tracking to sequential Sentinel-1a imagery (Joughin et al., 2010; Luckman et al., 2015). The ground-range aspect ratio of the single-look data is ~1:5, so the correlation window size of 500 × 100 pixels covers a ground area of ~1 × 1 km. Velocity is sampled every ~100 m in ground range (50 × 10 pixels). Surface crevasses are the most likely features to exhibit useful correlations between images, while speckle is probably rarely correlated over 12 days at this location because of highly variable temperatures and relatively high flow rates. To characterize the terminus speed at Kongsbreen, we calculate the median speed within a 500 × 500 m region (Figure 2b, white square) just upglacier of the terminus and equidistant from the fjord walls.

3.4. Constraining the Dry Calving Rate

As noted in previous studies, there is not a straightforward division between submarine melt driven calving and any other type of calving (Benn et al., 2017; O'Leary & Christoffersen, 2013; Seale et al., 2011). Here we use the same distinction of *dry* (melt-free) versus *wet* (melt-driven) calving as in O'Leary and Christoffersen (2013).

Observationally, it is difficult to measure the calving behavior of the glacier without the ubiquitous presence of frontal melting, and we therefore exploit the seasonal hydrologic cycle to constrain the dry calving rate. To quantify the dry calving rate, we select a time period when glacier runoff is minimal ($\dot{m}_{MW} \approx 0$) and the terminus is also free to calve (no buttressing due to the wintertime sea ice). We use a reanalysis runoff time series for Kongsbreen in combination with the timing of Sentinel-1a image acquisition and define the early melt season as 10 April to 16 May (day 101–137). During this period glacier runoff is zero, therefore we set $\dot{c}_{MW} = 0$ and equation (3) simplifies to $\dot{c}_{total} = \dot{c}_d + \dot{c}_{free} + \dot{c}_{circ}$. In using equations (4) and (5), this equation expands to become $\dot{c}_{total} = \dot{c}_d + \omega_f(\dot{m}_{free} + \dot{m}_{circ})$.

To constrain the calving amplification factor, ω_f, we focus on the calving style of Kongsbreen during the early melt season period. Previous work proposed that small flake calving events likely result from no amplification, whereas large calving events result from large undercuts with calving amplification (Benn et al., 2017). During the early melt season, we find the calving events to be frequent (~1 event every 5 hr) and small, representative of calving with little to no amplification (Benn et al., 2017). Therefore, we set $\omega_f = 1$ (i.e., no amplification) to compute $\dot{c}_{free}$ and $\dot{c}_{circ}$, and then solve for the dry calving rate. We find the dry calving rate to be 0.18 m/day, and hold it constant throughout the melt season (as in O'Leary & Christoffersen, 2013).

3.5. Calculating Submarine Melt Rates

3.5.1. Free Convection Melt Rate ($\dot{m}_{free}$)

We quantify the free convection melt rate, $\dot{m}_{free}$ (m/day), using a modified version of the empirical expression of El-Tahan et al. (1987; as in Kubat et al., 2005; Moon et al., 2017):

$$\dot{m}_{free} = 7.62\times10^{-3}T_d + 1.3\times10^{-3}T_d^2, \tag{8}$$

where the thermal driving temperature, T_d (°C), is calculated as the difference between ocean temperature and the freezing point of ocean water (Josberger, 1977). For ocean temperature, we use subsurface fjord temperature data collected from a mooring in Kongsfjorden (78.96°N, 11.80°E; Figure 2a, blue circle) ~16 km from the Kongsbreen glacier terminus in an ~200 m deep fjord (as used by Luckman et al., 2015). The mooring supported 10 temperature sensors spanning the 200 m depth, with approximately six sensors between 30 and 80 m, spaced at 10-m intervals. We choose a maximum depth of 80 m based upon the probable water mass exchange between the inner (glacier terminus) and outer (mooring location) fjord, as a 50 m sill stands between the mooring and the terminus of Kongsbreen (MacLachlan et al., 2016). Ocean temperature was measured throughout the duration of the 2016 melt season, with the exception of a 12-day gap (day 233–244) for instrument maintenance and data recovery. We use the mean daily ocean temperature, with a precision better than 0.1 °C after calibration (described by Cottier et al., 2005), and then average these daily temperatures to calculate the mean ocean temperature between Sentinel image acquisition dates. We calculate the average freezing temperature $(\overline{T}_{fp})$ of the ocean water by averaging the local freezing point, T_{fp}, between 30 and 80 m depth, using the equation:

$$T_{fp} = \lambda_1 S + \lambda_2 + \lambda_3 z_b, \tag{9}$$

where S is the ambient salinity, z_b is the ambient pressure (dbar), and λ_1 (-5.73×10^{-2} °C/psu), λ_2 (8.32×10^{-2} °C), and λ_3 (-7.61×10^{-4} °C/dbar) are constants. For the ambient salinity, S, we use in situ measurements of salinity between 30 and 80 m (average of 34.5 PSU), collected in Kongsfjorden from a ship-based CTD cast on 23 August 2016 (Figure 2a, red circle), and calculate $\overline{T}_{fp}$ to be −1.93 °C. Based upon the average freezing temperature, we then calculate the thermal driving temperature, T_d, for each 12-day period between the 2016 Sentinel images, and determined the corresponding free convection melt rate using equation (8).

3.5.2. Fjord Circulation Melt Rate ($\dot{m}_{circ}$)

To calculate the melt rate due to horizontal fjord circulation ($\dot{m}_{circ}$), we use the simplified version of the three equation formulation for melt due to turbulent water motion (e.g., Hellmer & Olbers, 2004; Holland & Jenkins, 1999) proposed by McPhee (1992) and subsequently used by Jenkins (2011). For this calculation, we assume that water is moving horizontally along the terminus rather than vertically up the face as in plume models.

$$\dot{m}_{circ} L_i + \dot{m}_{circ} c_i \left(\overline{T}_{fp} - T_i\right) = c_w C_d^{1/2} \Gamma_{TS} \vartheta_w T_d, \quad (10)$$

and L_i (3.35×10^5 J/kg) is the latent heat of fusion of ice, c_i (2009 J/(kg °C)) and c_w (3974 J/(kg °C)) are the specific heat capacities of ice and ocean water, T_i is the ice temperature (−2 °C) based on full-thickness temperature profiles collected at nearby glaciers (Björnsson et al., 1996), $C_d^{1/2}\Gamma_{TS}$ is the Stanton number (5.9×10^{-4}; Jenkins et al., 2010), ϑ_w is the water velocity relative to the glacier terminus (m/s), and T_∞ is the far field temperature measurement (°C). We modify the original conservation of heat equation by replacing T_∞ with T_d (°C) to include salinity (as in Moon et al., 2017).

In lieu of deploying instruments with a high likelihood of failure due to mélange, sea ice, and iceberg movement, we quantify the velocity of near-terminus fjord surface circulation (ϑ_w) by measuring the movement of natural trackers (icebergs) using time-lapse imagery. We installed a time-lapse camera at ~325 m above sea level on the north side of the fjord (Figure 2b, green circle), which acquired photographs at a temporal resolution of 30 min from 30 April to 15 September 2016 (day 121–259). This time frame spans the disintegration of the wintertime mélange and sea ice in the spring, through the peak of the melt season in summer, to the development of the wintertime mélange in early fall. To postprocess the time-lapse imagery, we use a MATLAB georectification package (available at https://gitlasso.uqar.ca/bourda02/g_rect) specifically designed to georectify oblique terrestrial imagery. We first stabilize the time-lapse images using foreground and distant bedrock for image alignment, which accounts for any slight movements or change in the camera's position caused by wind or camera servicing during image collection. We then orthorectify the imagery using ground-control points (GCPs) of known bedrock and terminus position coordinates visible in simultaneous ASTER (Advanced Spaceborne Thermal Emission and Reflection Radiometer; 15 m) and time-lapse camera imagery (Figures 3a and 3b). Next we reproject the orthorectified images onto a 2-m grid in UTM coordinates, thus enabling analysis of iceberg movement as if viewed from nadir (Figure 3c). We use additional ASTER satellite imagery to validate the initial georectification and use ASTER and Landsat-8 imagery throughout the time series to validate iceberg identification and terminus position. Lastly, we use the MATLAB image georectification and feature tracking toolbox, ImGRAFT (Messerli & Grinsted, 2015), to calculate the movement of small icebergs within 50 m of the glacier terminus and within the center ~1.3 km of the fjord (Figure 2b, black box) to avoid any boundary affects from the fjord walls. The errors associated with using ImGRAFT to calculate iceberg velocity are based upon uncertainties in the template matching, pixel coordinates of features, and resolution of the digital elevation model (DEM). For this study, we did not reproject the imagery onto a DEM as we were solely concerned with the fjord region, which is not susceptible to large variations in surface topography. We also have strongly constrained viewing geometry, therefore the errors resulting from feature tracking are due solely to template matching. We calculate this error by computing the velocity of a stationary area of bedrock over a 24-hr period (48 image pairs), thereby including any tracking errors due to illumination. We find the average velocity of the stationary bedrock to be 2.56×10^{-4} m/s, and thus also the error associated with iceberg velocity.

To derive water velocity from iceberg movement and remove the influence of wind, we apply the *2% rule* where the movement of small icebergs due to the wind is approximately 2% of the wind velocity, relative to the ocean currents (e.g., Garrett, 1985; Smith, 1993; Wagner et al., 2017). To justify the use of this approximation, the icebergs must fall into the *small* category ($l \times w \times h$ defined as $<100 \times 67 \times 67$ m; Bigg et al., 1997). To confirm Kongsbreen's icebergs meet this requirement, we determine a characteristic iceberg shape and volume using two WorldView-2 DEMs (2 m) collected at the peak of the 2015 melt season (3 July and 30 July). We first digitize the perimeter of 20 icebergs in open water, near the glacier terminus, and using the freeboard, calculate the volume of each iceberg using a density of 1,026 kg/m^3 for the ocean water (Svendsen et al., 2002) and an ice density of 900 kg/m^3 (Enderlin & Hamilton, 2014). The characteristic Kongsbreen iceberg has a mass of ~2.9×10^8 kg, and average surface dimensions of ~34×34 m, with a depth of 64 m based on a cylinder geometry. Kongsbreen icebergs therefore fall within the small category supporting the use of the 2% rule. However, 2% of the median recorded wind speed (2.7 m/s, 2% = 0.0054 m/s), measured at the Ny-Ålesund automatic weather station (AWS; 78.92°N, 11.93°E, 15 m above sea level; Figure 2a, orange circle), fell within our range of measured iceberg velocities (discussed in section 4.3) and we therefore consider $\vartheta_i = \vartheta_w$ in all subsequent calculations (i.e., we assume the water velocity is equal to the velocity of the tracked iceberg).

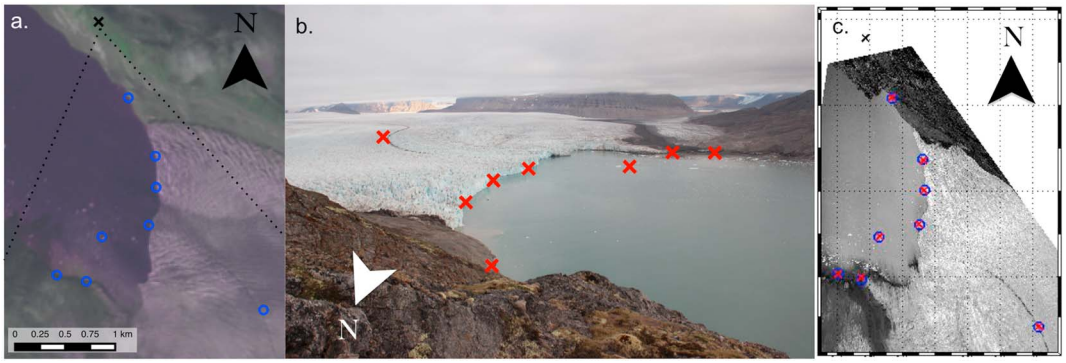

Figure 3. Corresponding Kongsbreen ground control points (GCPs) in the ASTER image (a, blue circles, 26 July 2016 12:30) and time-lapse camera image (TLC; b, red crosses, 26 July 2016 12:33) used to orthorectify the time-lapse imagery for the 2016 summer season. The georectified time-lapse image (c) shows the ASTER GCP coordinates (blue circles) lining up with the corresponding time-lapse camera GCP positions (red crosses), indicating a well-constrained georectification.

3.5.3. Meltwater Discharge Melt Rate ($\dot{m}_{MW}$)

To calculate the meltwater discharge melt rate ($\dot{m}_{MW}$), we use a modified version of the relationships established in Slater et al. (2016) for meltwater discharge from a distributed subglacial hydrology network:

$$\dot{m}_{MW(dist.)} = \frac{A_1[1 + A_2(T_{ocean} - T_{MW})]Q_{AVG}^{1/3}h}{l}, \tag{11}$$

and from a channelized subglacial network:

$$\dot{m}_{MW(channel.)} = \frac{A_3[1 + A_4(T_{ocean} - T_{MW})]Q_{AVG}^{1/3}h^{5/3}}{l}. \tag{12}$$

Here T_{MW} is the calculated pressure melting point temperature of meltwater discharging from under the glacier (−0.147 °C, equation in Cuffey & Paterson, 2010), Q_{AVG} is the average subglacial discharge (m^3/s) between Sentinel images, h is the height of the terminus under water (140 m), and l is the terminus length experiencing melting (m). For the distributed case, l = 1, 336 m, and for the channelized case, l = 200 m, based upon previous observations of submarine channel size (Jackson et al., 2017). The constants A_1, A_2, A_3, and A_4 are from Slater et al. (2016) with values of $1.56 \times 10^{-5} s^{-2/3}$, 0.84/°C, $4.05 \times 10^{-6} m^{1/3} s^{-2/3}$, and 0.75/°C, respectively.

To calculate Q, we use a reanalysis model which simulates runoff from the entire Kongsfjorden basin using an energy balance model coupled with a subsurface snow model (Van Pelt and Kohler, 2015). We derive the individual catchment around Kongsfjorden with a topographically controlled flow algorithm (Schwanghart & Kuhn, 2010) and determine the tidewater glacier catchment with hydraulic head calculations. The surface energy balance model computes melt by considering all the energy fluxes present in the Kongsbreen glacier environment. We use local air temperature, air pressure, relative humidity, and cloud cover from the Ny-Ålesund AWS (Figure 2a, orange circle, AWS), and precipitation from downscaled ERA-Interim reanalysis (Østby et al., 2017) to force the model. Meltwater produced at the surface enters the snowpack where it is allowed to refreeze or be stored as irreducible water depending upon the density, temperature, and available pore spaces of each of the 100 vertical layers. All residual meltwater, which has penetrated the entirety of the vertical layers and has reached the interface between snow and ice, is able to penetrate the remainder of the ice through crevasses, and therefore is considered subglacial meltwater runoff. We assume that there is no subglacial storage of water and that all water reaches the terminus by traveling along the steepest slope and without significant delay on a daily scale.

Table 1
Calculated Calving Rates, Melt Rates, and Velocities for the 2016 Melt Season at Kongsbreen With the Sentinel Image Pairs (Column 1) Determining Wach Sampling Period

Image pairs (day of year)	ϑ_g (m/day)	dP/dt (m/day)	$\dot{c}_{total}$ (m/day)	T_{ocean} (°C)	T_d (°C)	Q_{avg} (m^3/s)	$\dot{m}_{free}$ (m/day)	$\dot{m}_{circ}$ (m/day)	$\dot{c}_f$ (m/day)	$\dot{m}_{MW(200)}$ (m/day)	$\dot{m}_{MW(1336)}$ (m/day)	$\dot{c}_{resid}$ (m/day)
101–137	0.99	+0.71	0.28	1.69	3.62	0	0.04	0.06	0.10	0	0	0
137–149	1.20	+0.80	0.40	2.73	4.66	0.01	0.06	0.07	0.13	0.10	0.10	0.09
149–161	1.32	+0.65	0.67	3.19	5.12	0.97	0.07	0.08	0.15	0.52	0.53	0.34
161–185	0.11	−0.93	1.04	3.73	5.66	12.24	0.08	0.09	0.17	1.35	1.39	0.69
185–197	0.86	−0.70	1.56	3.97	5.90	26.67	0.09	0.09	0.18	1.82	1.88	1.20
197–209	0.53	−1.70	2.23	4.64	6.57	26.73	0.11	0.10	0.21	2.05	2.12	1.84
209–221	0.57	−5.91	6.48	4.31	6.24	18.42	0.10	0.10	0.20	1.71	1.77	6.10
221–233	0.63	−4.51	5.14	4.76	6.69	20.26	0.11	0.11	0.22	1.91	1.97	4.74
233–245	0.37	−6.61	6.98	4.86	6.32	4.94	0.10	0.10	0.20	1.21	1.25	6.60
245–257	0.62	−3.51	4.13	4.85	6.78	1.01	0.11	0.11	0.22	0.71	0.74	3.73
257–269	1.39	−2.61	4.00	5.17	7.10	4.71	0.12	0.11	0.23	1.25	1.29	3.59
269–281	1.18	−2.46	3.64	5.23	7.17	2.87	0.12	0.11	0.23	1.07	1.11	3.23

Note. Days of Sentinel imagery (column 1) are used to calculate glacier velocity (column 2), the change in terminus position (column 3), and the total calving rate (column 4). Ocean temperatures collected at a mooring (column 5), adjusted ocean temperatures calculated using measurements from a CTD cast (column 6), and glacier runoff (column 7) are used to calculate melt rates due to free convection (column 8) and fjord circulation (calculated with average observed ocean velocities, column 9). The combined calving rate due to free convection and fjord circulation (column 10) assumes an amplification factor (ω_f) of 1, and the residual calving rate (column 13) is calculated by subtracting the calving due to free convection and fjord circulation (column 10) and the dry calving rate (0.18 m/day) from the total calving rate (column 4). Melt rates due to meltwater discharge are calculated for a focused channel (column 11) assuming all discharge emerges from the central 200 m of the glacier terminus and a distributed subglacial hydrology network (column 12) assuming discharge is emerging across the entire 1,336 m of the glacier terminus.

4. Results

4.1. Glacier Velocity and Calving Rates

Applying feature tracking to the Sentinel imagery, we found glacier velocities ranged from 0.11 to 1.39 m/day (Table 1), which, combined with terminus position changes in equation (7), corresponds to a total calving rate ($\dot{c}_{total}$) between 0.28 and 6.98 m/day (Table 1). We solved equation (3) for each time period, where $\dot{c}_d = 0.18\mathrm{m/day}$, $\omega_f = 1$, and equations (8) and (10) are used to calculate the melt rate due to free convection

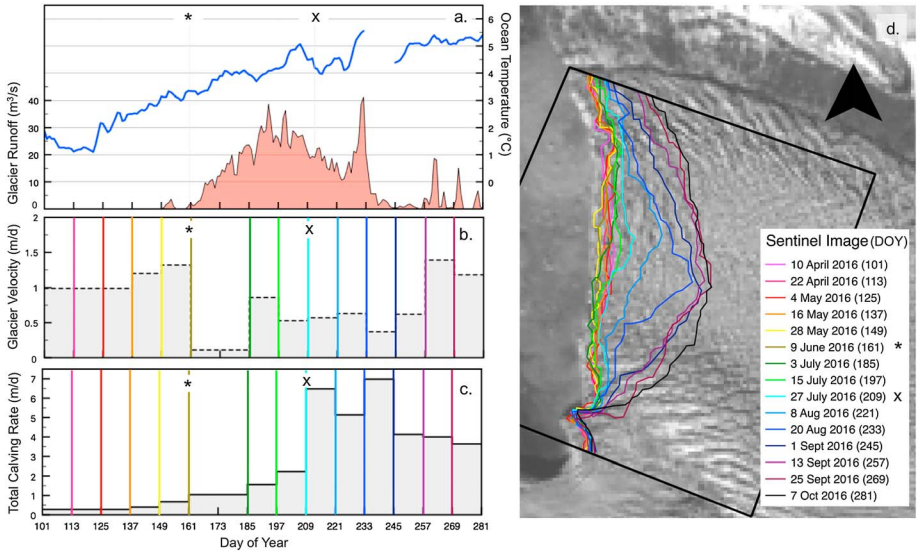

Figure 4. Plot of the daily average ocean temperature between 30 and 80 m depth (a, blue line) and glacier runoff (a, pink fill), in comparison with glacier velocity (b) and total calving rate (c) between sequential Sentinel images over the 2016 melt season. Colors of vertical lines (b and c) correspond to digitized terminus position on the Kongsbreen image map (d). The asterisks represents a decrease in glacier velocities, and the cross represents a jump in the calving rate due to meltwater discharge and a transition to calving focused at the meltwater discharge location.

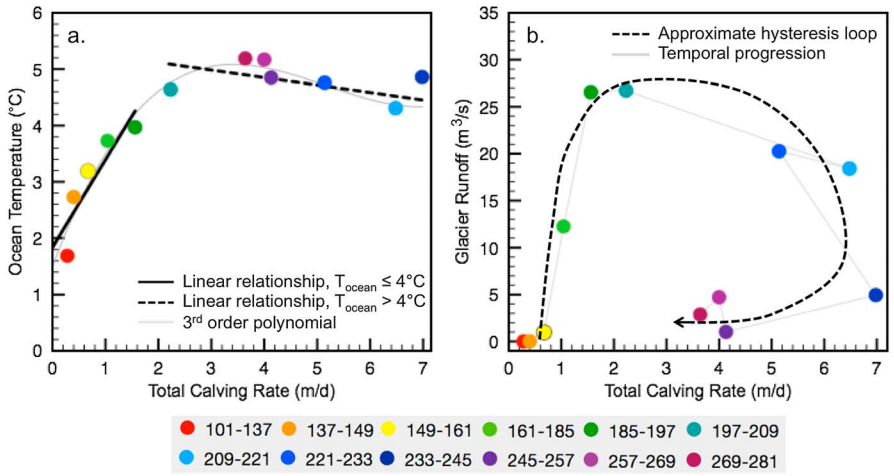

Figure 5. Average ocean temperature (from a depth of 30 to 80 m; a) and average glacier runoff (b) between sequential Sentinel images (colored circles) plotted against the total calving rate. Linear (a, black lines) and third-order polynomial (a, solid gray line) lines show the strongest relationship between the total calving rate and the ocean temperature. The hysteresis loop (b, dashed black line) suggests a variable calving response to glacier runoff, which is temporally dependent. The transition to calving focused at the prominent meltwater discharge location occurs on day 209, the same time the relationship between the total calving rate and glacier runoff transitions from linear to a hysteresis loop.

and fjord circulation, respectively. The contribution to total glacier calving rate from free convection and fjord circulation ($\dot{c}_f$) ranged from 0.10 to 0.23 m/day. The remainder of the total calving rate, 0–6.60 m/day (residual calving rate, $\dot{c}_{resid}$), we attribute to meltwater discharge calving ($\dot{c}_{MW}$). At the peak of calving, the calving rates attributed to meltwater discharge was an order of magnitude greater than the calving rate attributed to free convection and fjord circulation calving combined. Flake icebergs (<1,000 m^2, average ~250 m^2) dominate calving early in the melt season, and a combination of flakes and larger icebergs (~450 m^2) are produced as the predominant area of iceberg calving transitions to the subglacial discharge location in the late-season (July–August, Figure 4d).

4.2. Total Calving Rate Versus Ocean Temperature and Glacier Runoff

In comparing the total glacier calving rate (0.28–6.98 m/day) to concurrent average ocean temperatures from 30 to 80 m depth (1.69–5.23 °C), we find an approximately linear relationship between these variables with a break at ~4 °C (Figure 5a). Data points with an ocean temperature less than 4 °C have a slope of ~1.5 (R^2 = 0.80), similar to nearby Kronebreen (Luckman et al., 2015), and data points with an ocean temperature greater than 4 °C have a slightly negative slope (R^2 = 0.38). If we fit a third order polynomial to these data instead of two linear trend lines, we find a strong correlation (R^2 = 0.95, Figure 5a, solid gray line), however, a polynomial fit is nonsensical outside the range of observations, so we therefore use ocean temperature to divide the linear relationships. When comparing the total glacier calving rate with modeled glacier runoff results (Figure 5b), we find no consistent relationship, but a temporally distinct hysteresis loop (Figure 5b, dashed black line) where the same rate of glacier runoff late in the season has a larger associated calving rate than early in the melt season. The amplified calving late in the season also coincides with the highest ocean temperatures recorded during the study period (Figure 4a) and a shift from calving occurring across the terminus width to focused calving at the submarine discharge location (Figure 4d). These concurrent changes suggest that the meltwater discharge melt rate, timing of meltwater discharge, and the temperature of the ocean are critical parameters to the total glacier calving rate.

4.3. Water Velocities From Iceberg Motion

To quantify water flow direction and speed, we measure iceberg motion close to the terminus of Kongsbreen. Using the iceberg feature tracking results from the georectified time-lapse camera imagery, we identify four prominent states of iceberg movement, and therefore water flow, in the near-terminus region:

1. Along-fjord flow: characterized by surface water moving either up-fjord or down-fjord as a collective unit. Such flow is generally related to large calving or wind events, and on very few occasions is coincident with the subdiurnal tide.
2. Isolated along-terminus flow: characterized by surface water moving parallel to the glacier terminus on a local scale (less than the full terminus width). Such flow generally occurred at locations adjacent to calved icebergs or sites of subglacial discharge and immediately following a calving event or subglacial discharge pulse.
3. U-turn flow: characterized by surface water moving toward the glacier on one side of the fjord, contacting the glacier, redirecting to flow parallel to the terminus, impacting the opposite fjord wall, and flowing toward the ocean on the opposite side of the fjord. The along-terminus flow occupied the entire width of the fjord, and the entry and exit sides were variable.
4. Eddy circulation: characterized by closed-loop circulation of surface waters in a clockwise or counterclockwise orientation adjacent to the terminus. The spatial and temporal variability ranges from 10s of meters in diameter lasting minutes to hours, to full-fjord-width circulation lasting several hours.

For the remainder of this paper, we use velocities adjacent to the terminus calculated only during eddy circulation events (iceberg movement state 4), occupying the full-fjord width, and consider this range of velocities as characteristic of all fjord circulation velocities present throughout the melt season. We choose this circulation pattern as it encompasses all of the prominent states of iceberg movement (e.g., flow along-terminus, into the terminus, away from the terminus, and circulation back toward the terminus) and therefore is an appropriate representation of average fjord circulation. The eddy circulation events lasted between 3.5 and 15 hr, with an average iceberg velocity of $2.6 \times 10^{-2} \pm 2.56 \times 10^{-4}$ m/s (range of 1.6×10^{-2} to 3.6×10^{-2} m/s). While the water velocity is variable throughout a melt season and likely with depth, we apply this range of water velocities across the entire study period and with fjord depth to establish a maximum melt rate and terminus undercutting due to fjord circulation.

5. Discussion

5.1. Calculating Meltwater Discharge Calving Rate ($\dot{c}_{MW}$)

To calculate the calving rate due to meltwater discharge, we quantify the melt rate due to meltwater discharge ($\dot{m}_{MW}$) and constrain the calving amplification factor (ω_{MW}). We use the relationships established in equations (11) and (12) to first calculate the meltwater discharge melt rate (Figure 6, solid green and purple lines) and compare this melt rate to the residual calving rate (Figure 6, solid red line). We find a stark difference between the meltwater discharge melt rates and the residual calving rate before and after day 209 (Figure 6). After day 209, the meltwater discharge melt rates (Figure 6, solid green and purple lines) are drastically lower than the residual calving rate (Figure 6, solid red line), therefore calving amplification is likely occurring and $\omega_{MW} \neq 1$. A calving amplification physically represents ice loss extending beyond the submarine melt undercut. The calving record supports this implication, as larger icebergs calve as soon as calving becomes focused at the meltwater discharge location.

For Kongsbreen, we found the highest correspondence between the residual calving rate and the computed meltwater discharge calving rate when $\omega_{MW(200)} = 3$, and we shifted the meltwater calving rate forward by 12 days (accounting for a proposed temporal lag of 12 days; modification indicated by asterisks in Figure 6). While this shift and calving amplification may more closely characterize the residual calving rate than no shift or calving amplification, the modification still overestimates the early season calving and underestimates the late season calving (Figure 6, black dashed line). This misrepresentation could be, in part, due to the hysteresis relationship between glacier runoff and total glacier calving rate (Figure 5b). Early in the melt season, the lag between an increase in meltwater runoff and calving response may represent the time needed for the submarine undercut notch to develop (e.g., Fried et al., 2015; Rignot et al., 2015; Slater et al., 2017). However, in both the distributed and channelized subglacial discharge configurations used to calculate the meltwater calving rates, an overestimation of calving early in the melt season is observed. Processes not driven by submarine melting could be contributing to the late season offset, such as calving resulting from destabilized terminus geometry (e.g., from focused calving). However, the complex relationship between meltwater discharge melt rates, ocean temperatures, and meltwater discharge calving rates is also likely not fully represented in this simplified amplification

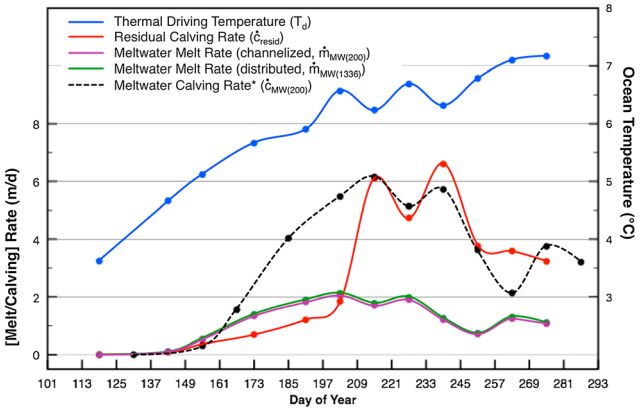

Figure 6. Melt rate (green and purple solid lines) and potential calving rate trend (black dashed line) due to meltwater discharge and thermal driving temperature of the ocean (blue line). While both calving rate trends closely follow one another, the green line assumes discharge across the entire width of the glacier (1,336 m) and an amplification factor dependent on the differential ocean temperature (T_d), while the purple line assumes all discharge is focused at one opening (200 m wide) and a constant amplification factor independent of ocean temperature. The calving rate is shifted forward by 12 days (indicated by asterisks) to better correspond with the residual calving rate (red line) trend.

factor. Nevertheless, this calving response justifies the partitioning of the calving rate into free convection, fjord circulation, and meltwater discharge.

5.2. Calving Rates and Environmental Controls

In comparing the records of partitioned calving rates and glacier velocity (Figure 7), there are two distinct transitions in the synthesis of these time series. The first is the significant drop in glacier velocity (day 161), which also marks the transition from fairly consistent winter-time velocities to variable summer velocities. This occurred 35 days after the breakup of the wintertime sea ice (day 126, 5 May 2016) and between 12 and 24 days after the total glacier calving rate transitioned from being dominated by free convection and fjord circulation calving to residual (meltwater) calving (day 161, asterisk, Figures 4 and 7; Table 1). The combination of increased meltwater calving and decreased glacier velocities could signify the transition between a distributed subglacial configuration to a more connected, efficient, subglacial network (as observed by Nienow et al., 1998). The second transition occurs when the residual calving rate spikes, and calving begins to focus at the meltwater discharge location (day 209, cross, Figures 4 and 7).

5.3. Caveats and Uncertainties

The methods developed and successfully used here are easily generalized to other tidewater glaciers; however, the dynamics they reveal may vary from glacier to glacier. Kongsbreen has one dominant discharge location, and therefore the majority of meltwater is likely routed to this central location amplifying the single impact of meltwater discharge on terminus geometry. However, if Kongsbreen had multiple dominant discharge locations, meltwater discharge would still influence terminus shape as localized melting would continue, but the overall impact of each individual discharge location would be dampened and a single focused calving location, as observed here, likely would not occur.

The shallow depth of Kongsbreen's fjord (~140 m) likely allows subglacial meltwater to rise more frequently to the surface, thereby melting the entire height of the terminus face during the meltwater transit. In deeper fjords, the meltwater has a greater vertical distance to travel before reaching the surface, so the probability of meltwater equilibrating at depth is greater, thus only allowing terminus melt for a portion of the terminus thickness (e.g., Carroll et al., 2016; Chauché et al., 2014). Meltwater equilibration at depth is also one of the proposed mechanisms for development of subsurface layers, which would also encourage equilibration (Sciascia et al., 2013; Sole et al., 2011; Straneo et al., 2011). Therefore, it may be that the meltwater discharge amplification factor (ω_{MW}) decreases with increasing fjord depth. Conversely, tidewater glaciers draining into deeper fjords may also have a larger catchment basin, such as those in Greenland, and therefore greater meltwater discharge; this would enable a more expedient development of a submarine notch and allow meltwater to impact the glacier for a longer portion of the melt season. In this case, increased meltwater discharge would encourage more efficient terminus melting and subsequent calving (Luckman et al., 2015; Motyka et al., 2013).

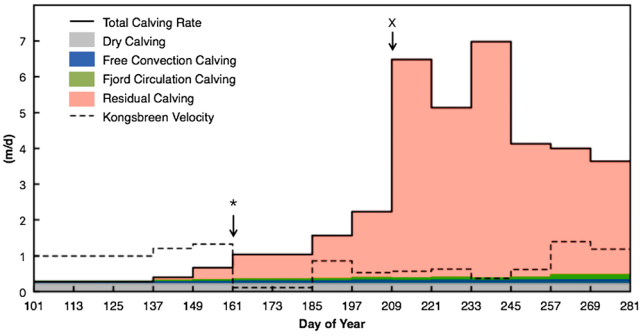

Figure 7. Kongsbreen velocity (m/day, dashed black line) and total calving rate (m/day, solid black line) for the 2016 summer melt season derived from Sentinel-1a imagery. Colored bars indicate the partitioning of the total calving rate into the dry calving rate (gray bar), and the calving rates of free convection (blue bar), fjord circulation (green bar), and residual (pink bar), attributed largely to meltwater discharge calving. The asterisk represents a large decrease in glacier velocity, while the cross notes a large spike in the residual (meltwater) calving rate (as shown in Figure 5).

Several assumptions were made in parameterizing melt rates, specifically those associated with fjord circulation. Many of the assumptions were made to establish the maximum contribution of fjord circulation melt on total glacier calving rate. These assumptions include the full-submerged thickness of the glacier terminus experiencing the same along-terminus flow as at the surface, the water velocities associated with full-fjord-width circulation events representing the average circulation along the terminus,

and the calculated water velocities occurring throughout the entire melt season. All of these assumptions are unlikely to be entirely justified due to the subglacial discharge and fjord mixing present at Kongsbreen, and thus these calculations likely overestimate fjord melting. Nevertheless, even as an overestimate, fjord melting still remains a relatively small contributor to the total glacier calving rate.

Lastly, while we attempted to present a conservative estimate of calving due to meltwater discharge by maximizing calving rates due to fjord circulation, we only include the three simplified mechanisms of submarine melting and terminus undercutting. We therefore recognize that the residual calving rate may likely include yet unidentified forms of submarine melt mechanisms in addition to meltwater discharge calving, such as tides. However, we saw very few instances of coincident iceberg movement with tidal phase in the time-lapse camera time series and therefore rule it out as a dominant control at Kongsbreen. We note that, for simplicity, several other relationships of potential importance have been ignored, such as the interplay between the three mechanisms of submarine melting, specifically meltwater discharge-driven horizontal fjord circulation, as well as changes in the dry calving rate of the glacier resulting from glacier thinning or crevasses filling with water. The inclusion of these additional mechanisms or changes in the glacier surface would decrease the residual calving rate, and subsequently the calving rate due to meltwater discharge. Additionally, the melt rate calculations presented here currently rely on parameterizations not very well tested observationally and/or only derived in numerical models. More in situ studies and laboratory experiments are needed to physically support these equations.

6. Conclusions

During this study we partitioned total glacier calving rate into calving resulting from three forms of submarine melting: free convection, horizontal fjord circulation, and meltwater discharge. We used a variety of in situ and remote sensing data to quantify submarine melt rates including time-lapse camera and Sentinel imagery collected during the 2016 melt season at Kongsbreen, Svalbard, as well as mooring data for mid-fjord ocean temperature (30–80 m depth), a CTD cast, and reanalysis runoff results. To calculate water velocity, we used the time-lapse imagery to capture icebergs moving along the terminus. We orthorectified and geolocated the time-lapse imagery and, through the 30-min temporal resolution, were able to track iceberg movement near the terminus corresponding to water velocities between 1.6×10^{-2} and $3.6 \times 10^{-2} \pm 2.56 \times 10^{-4}$ m/s. We used full-fjord width (eddy) circulation events as a benchmark for persistent along-terminus flow, and found fjord circulation accounts for a maximum of 0.06–0.11 m/day of terminus undercutting with the melt rate due to fjord circulation of comparable magnitude to free convection melt rates (0.10–0.22 m/day). In quantifying the calving rate due to free convection and fjord circulation (0.10–0.23 m/day), we isolated the residual calving rate, due largely to meltwater discharge, finding this calving rate to be 0–6.60 m/day, or up to an order of magnitude larger than the combined calving rate due to free convection and fjord circulation. We calculated the melt rates due to meltwater discharge in a channelized and distributed subglacial hydrology configuration, finding melt rates between 0 and 2.05 m/day when focused across 200 m (channelized) or 0 and 2.12 m/day when discharging across the entire 1,336 m width of the terminus (distributed).

In this study, we observed an increase in the contribution of meltwater discharge calving to overall calving rate in parallel with an increase in meltwater discharge and ocean temperature (Figures 4 and 7), which supports our hypothesis, and ideas previously proposed by others, that meltwater discharge is a dominant control on terminus shape and retreat (e.g., Fried et al., 2015; Motyka et al., 2013; Rignot et al., 2015; Truffer & Motyka, 2016). Due to the variable relationship between meltwater discharge melt rate and the residual calving rate, we propose an amplification factor of 3 and a temporal lag of 12 days (Figure 6). However, we were still unable to completely fit the meltwater discharge calving rate to the residual calving rate, likely due to the hysteresis relationship between glacier runoff and total glacier calving rate (Figure 5b). Therefore, lacking an ideal correspondence between melt rate and calving rate, using calving rates to assess the impact of meltwater discharge on glacier terminus stability could provide a more fruitful alternative to directly calculating melt rates. Due to the influence of meltwater on terminus position and shape, and the dominant control meltwater discharge and ocean temperatures have on total glacier calving rates, continued investigations into the controls on submarine melting are critical. Additionally, incorporation of these relationships into models is essential to accurately predicting the future of glaciers as atmospheric and oceanic temperatures, and thus meltwater discharge, continue to rise.

Acknowledgments

We would like to thank the New Hampshire Space Grant Consortium (award # NNX15AH79H) for the training grant to fund KMS; the ConocoPhillips-Ludin Northern Area Program (under the CRIOS project) and the Dartmouth Graduate Studies Travel fund for their financial support to conduct fieldwork and travel for data dissemination; the Polar Geospatial Center for arranging access to the WorldView-2 imagery; the UK Natural Environmental Research Council (NERC) Oceans 2025 and Northern Sea Program for mooring work support, with further support from the Research Council of Norway (NFR) projects: Circa (214271), Cleopatra (178766), Cleopatra II (216537), and Marine Night (226471); Alex Hart and the GeoSciences Mechanical Workshop at the University of Edinburgh for manufacturing the time-lapse camera enclosure that was used in this study; Colin Griffiths (SAMS) and Jørgen Berge (UiT) for overseeing the collection of mooring data in Kongsfjorden since 2002; ESA for processing the Copernicus Sentinel data (2016). A video of the Sentinel imagery used in this study (doi:10.18739/A2NZ80P8K), as well as the raw time-lapse imagery (doi:10.18739/A2SQ8QH3F), mooring ocean temperature data, and CTD cast measurements (doi:10.18739/A2XG9F97K) are all available at the Arctic Data Center. Lastly, we would like to thank Bryn Hubbard and the four anonymous reviewers for their very helpful and thorough reviews.

References

Amundson, J. M., Fahnestock, M., Truffer, M., Brown, J., Luthi, M. P., & Motyka, R. J. (2010). Ice mélange dynamics and implications for terminus stability, Jakobshavn Isbræ Greenland. *Journal of Geophysical Research*, *115*, F01005. https://doi.org/10.1029/2009JF001405

Bassis, J. N., & Jacobs, S. (2013). Diverse calving patterns linked to glacier geometry. *Nature Geoscience*, *6*(10), 833–836. https://doi.org/10.1038/ngeo1887

Benn, D. I., Astrom, J., Zwinger, T., Todd, J., Nick, F. M., Cook, S., et al. (2017). Melt-under-cutting and buoyancy-driven calving from tidewater glaciers: New insights from discrete element and continuum model simulations. *Journal of Glaciology*, *63*(240), 691–702. https://doi.org/10.1017/jog.2017.41

Benn, D. I., Warren, C. R., & Mottram, R. H. (2007). Calving processes and the dynamics of calving glaciers. *Earth-Science Reviews*, *82*(3–4), 143–179. https://doi.org/10.1016/j.earscirev.2007.02.002

Bigg, G. R., Wadley, M. R., Stevens, D. P., & Johnson, J. A. (1997). Modelling the dynamics and thermodynamics of icebergs. *Cold Regions Science and Technology*, *26*(2), 113–135. https://doi.org/10.1016/S0165-232X(97)00012-8

Björnsson, H., Gjessing, Y., Hamran, S.-E., Hagen, J. O., Pálsson, F., & Erlingsson, B. (1996). The thermal regime of sub-polar glaciers mapped by multi-frequency radio-echo sounding. *Journal of Glaciology*, *42*(140), 23–32. https://doi.org/10.1017/S0022143000030495

Blaszczyk, M., Jania, J. A., & Hagen, J. O. (2009). Tidewater glaciers of Svalbard: Recent changes and estimates of calving fluxes. *Polish Polar Research*, *30*(2), 85–142.

Carroll, D., Sutherland, D. A., Hudson, B., Moon, T., Catania, G. A., Shroyer, E. L., et al. (2016). The impact of glacier geometry on meltwater plume structure and submarine melt in Greenland fjords. *Geophysical Research Letters*, *43*, 9739–9748. https://doi.org/10.1002/2016GL070170

Cenedese, C., & Linden, P. F. (2014). Entrainment in two coalescing axisymmetric turbulent plumes. *Journal of Fluid Mechanics*, *752*(R2), 12. https://doi.org/10.1017/jfm.2014.389

Chauché, N., Hubbard, A., Gascard, J. C., Box, J. E., Bates, R., Koppes, M., et al. (2014). Ice-ocean interaction and calving front morphology at two west Greenland tidewater outlet glaciers. *The Cryosphere*, *8*(4), 1457–1468. https://doi.org/10.5194/tc-8-1457-2014

Christoffersen, P., O'leary, M., Van Angelen, J., & van den Broeke, M. (2012). Partitioning effects from ocean and atmosphere on the calving stability of Kangerdlugssuaq Glacier, East Greenland. *Annals of Glaciology*, *53*(60), 249–256. https://doi.org/10.3189/2012AoG60A087

Cottier, F., Tverberg, V., Inall, M. E., Svendsen, H., Nilsen, F., & Griffiths, G. (2005). Water mass modification in an Arctic fjord through cross-shelf exchange: The seasonal hydrography of Kongsfjorden, Svalbard. *Journal of Geophysical Research*, *110*, C12005. https://doi.org/10.1029/2004JC002757

Cowton, T., Slater, D., Sole, A., Goldberg, D., & Nienow, P. (2015). Modeling the impact of glacial runoff on fjord circulation and submarine melt rate using a new subgrid-scale parameterization for glacial plumes. *Journal of Geophysical Research, Oceans*, *120*, 796–812. https://doi.org/10.1002/2014JC010324

Cuffey, K. M., & Paterson, W. S. B. (2010). *The physics of glaciers* (4th ed.). Amsterdam, Academic Press.

El-Tahan, M., Venkatesh, S., & El-Tahan, H. (1987). Validation and quantitative assessment of the deterioration mechanisms of Arctic icebergs. *Journal of Offshore Mechanics and Arctic Engineering*, *109*(1), 102–108. https://doi.org/10.1115/1.3256983

Enderlin, E. M., & Hamilton, G. S. (2014). Estimates of iceberg submarine melting from high-resolution digital elevation models: Application to Sermilik Fjord, East Greenland. *Journal of Glaciology*, *60*(224), 1084–1092. https://doi.org/10.3189/2014JoG14J085

Enderlin, E. M., Howat, I. M., & Vieli, A. (2013). High sensitivity of tidewater outlet glacier dynamics to shape. *The Cryosphere*, *7*(3), 1007–1015. https://doi.org/10.5194/tc-7-1007-2013

Fried, M. J., Catania, G. A., Bartholomaus, T. C., Duncan, D., Davis, M., Stearns, L. A., et al. (2015). Distributed subglacial discharge drives significant submarine melt at a Greenland tidewater glacier. *Geophysical Research Letters*, *42*, 9328–9336. https://doi.org/10.1002/2015GL065806

Garrett, C. (1985). Statistical prediction of iceberg trajectories. *Cold Regions Science and Technology*, *11*(3), 255–266. https://doi.org/10.1016/0165-232X(85)90050-3

Hellmer, H. H., & Olbers, D. J. (2004). A two-dimensional model for the thermohaline circulation under an ice shelf. *Antarctic Science*, *1*(04). https://doi.org/10.1017/s0954102089000490

Holland, D. M., & Jenkins, A. (1999). Modeling thermodynamic ice-ocean interactions at the base of an ice shelf. *Journal of Physical Oceanography*, *29*(8), 1787–1800. https://doi.org/10.1175/1520-0485(1999)029<1787:MTIOIA>2.0.CO;2

Holland, D. M., Thomas, R. H., De Young, B., Ribergaard, M. H., & Lyberth, B. (2008). Acceleration of Jakobshavn Isbræ triggered by warm subsurface ocean waters. *Nature Geoscience*, *1*(10), 659–664. https://doi.org/10.1038/ngeo316

How, P., Benn, D. I., Hulton, N. R. J., Hubbard, B., Luckman, A., Sevestre, H., et al. (2017). Rapidly changing subglacial hydrological pathways at a tidewater glacier revealed through simultaneous observations of water pressure, supraglacial lakes, meltwater plumes and surface velocities. *The Cryosphere*, *11*(6), 2691–2710. https://doi.org/10.5194/tc-11-2691-2017

Howat, I. M., Tulaczyk, S., Rhodes, P., Israel, K., & Snyder, M. (2007). A precipitation-dominated, mid-latitude glacier system: Mount Shasta, California. *Climate Dynamics*, *28*(1), 85–98. https://doi.org/10.1007/S00382-006-0178-9

Inall, M. E., Murray, T., Cottier, F. R., Scharrer, K., Boyd, T. J., Heywood, K. J., & Bevan, S. L. (2014). Oceanic heat delivery via Kangerdlugssuaq Fjord to the south-east Greenland ice sheet. *Journal of Geophysical Research: Oceans*, *119*, 631–645. https://doi.org/10.1002/2013JC009295

Jackson, R. H., Shroyer, E. L., Nash, J. D., Sutherland, D. A., Carroll, D., Fried, M. J., et al. (2017). Near-glacier surveying of a subglacial discharge plume: Implications for plume parameterizations. *Geophysical Research Letters*, *44*, 6886–6894. https://doi.org/10.1002/2017GL073602

Jackson, R. H., & Straneo, F. (2016). Heat, salt, and freshwater budgets for a glacial fjord in Greenland. *Journal of Physical Oceanography*, *46*(9), 2735–2768. https://doi.org/10.1175/JPO-D-15-0134.1

Jackson, R. H., Straneo, F., & Sutherland, D. A. (2014). Externally forced fluctuations in ocean temperature at Greenland glaciers in non-summer months. *Nature Geoscience*, *7*(7), 503–508. https://doi.org/10.1038/ngeo2186

Jenkins, A. (2011). Convection-driven melting near the grounding lines of ice shelves and tidewater glaciers. *Journal of Physical Oceanography*, *41*(12), 2279–2294. https://doi.org/10.1175/JPO-D-11-03.1

Jenkins, A., Dutrieux, P., Jacobs, S. S., McPhail, S. D., Perrett, J. R., Webb, A. T., & White, D. (2010). Observations beneath Pine Island glacier in West Antarctica and implications for its retreat. *Nature Geoscience*, *3*(7), 468–472. https://doi.org/10.1038/ngeo890

Josberger, E. G. (1977). *A laboratory and field study of iceberg deterioration, paper presented at Iceberg utilization for fresh water production, weather modification and other applications*. Ames, Iowa: Pergamon Press.

Joughin, I., Smith, B., & Abdalati, W. (2010). Glaciological advances made with interferometric synthetic aperture radar. *Journal of Glaciology*, *56*(200), 1026–1042. https://doi.org/10.3189/002214311796406158

Kimura, S., Holland, P. R., Jenkins, A., & Piggott, M. (2014). The effect of meltwater plumes on the melting of a vertical glacier face. *Journal of Physical Oceanography*, *44*(12), 3099–3117. https://doi.org/10.1175/JPO-D-13-0219.1

Kubat, I., Sayed, M., Savage, S. B., & Carrieres, T. (2005). An operational model of iceberg drift. *International Journal of Offshore and Polar Engineering*, *15*, 125–131.

Luckman, A., Benn, D. I., Cottier, F., Bevan, S. L., Nilsen, F., & Inall, M. E. (2015). Calving rates at tidewater glaciers vary strongly with ocean temperature. *Nature Communications*, *6*(1), 8566–8572. https://doi.org/10.1038/ncomms9566

MacLachlan, S. E., Cottier, F. R., Austin, W. E. N., & Howe, J. A. (2016). The salinity: δ18O water relationship in Kongsfjorden, western Spitsbergen. *Polar Research*, *26*(2), 160–167. https://doi.org/10.1111/j.1751-8369.2007.00016.x

Magorrian, S. J., & Wells, A. J. (2016). Turbulent plumes from a glacier terminus melting in a stratified ocean. *Journal of Geophysical Research: Oceans*, *121*, 4670–4696. https://doi.org/10.1002/2015JC011160

Mankoff, K. D., Straneo, F., Cenedese, C., Das, S. B., Richards, C. G., & Singh, H. (2016). Structure and dynamics of a subglacial discharge plume in a Greenlandic fjord. *Journal of Geophysical Research*, *121*, 8670–8688. https://doi.org/10.1002/2016JC011764

McPhee, M. G. (1992). Turbulent heat flux in the upper ocean under sea ice. *Journal of Geophysical Research*, *97*(C4), 5365. https://doi.org/10.1029/92JC00239

Messerli, A., & Grinsted, A. (2015). Image georectification and feature tracking toolbox: ImGRAFT. *Geoscientific Instrumentation Methods*, *4*(1), 23–34. https://doi.org/10.5194/gi-4-23-2015

Moon, T., & Joughin, I. (2008). Changes in ice front position on Greenland's outlet glaciers from 1992 to 2007. *Journal of Geophysical Research*, *113*, F02022. https://doi.org/10.1029/2007JF000927

Moon, T., Sutherland, D. A., Carrol, D., Felikson, D., Kehrl, L., & Straneo, F. (2017). Subsurface iceberg melt key to Greenland fjord freshwater budget. *Nature Geoscience*, *11*(1), 49–54. https://doi.org/10.1038/s41561-017-0018-z

Motyka, R. J., Dryer, W. P., Amundson, J., Truffer, M., & Fahnestock, M. (2013). Rapid submarine melting driven by subglacial discharge, LeConte Glacier, Alaska. *Geophysical Research Letters*, *40*, 5153–5158. https://doi.org/10.1002/Grl.51011

Nick, F. M., Vieli, A., Andersen, M. L., Joughin, I., Payne, A., Edwards, T. L., et al. (2013). Future sea-level rise from Greenland's main outlet glaciers in a warming climate. *Nature*, *497*(7448), 235–238. https://doi.org/10.1038/nature12068

Nick, F. M., Vieli, A., Howat, I. M., & Joughin, I. (2009). Large-scale changes in Greenland outlet glacier dynamics triggered at the terminus. *Nature Geoscience*, *2*(2), 110–114. https://doi.org/10.1038/ngeo394

Nienow, P., Sharp, M., & Willis, I. (1998). Seasonal changes in the morphology of the subglacial drainage system, Haut Glacier d'Arolla, Switzerland. *Earth Surface Processes and Landforms*, *23*(9), 825–843. https://doi.org/10.1002/(Sici)1096-9837(199809)23:9<825::Aid-Esp893>3.0.Co;2-2

O'Leary, M., & Christoffersen, P. (2013). Calving on tidewater glaciers amplified by submarine frontal melting. *The Cryosphere*, *7*(1), 119–128. https://doi.org/10.5194/tc-7-119-2013

Østby, T. I., Schuler, T. V., Hagen, J. O., Hock, R., Kohler, J., & Reijmer, C. H. (2017). Diagnosing the decline in climatic mass balance of glaciers in Svalbard over 1957 & 2014. *The Cryosphere*, *11*(1), 191–215. https://doi.org/10.5194/tc-11-191-2017

Rignot, E., Fenty, I., Xu, Y., Cai, C., & Kemp, C. (2015). Undercutting of marine-terminating glaciers in west Greenland. *Geophysical Research Letters*, *42*, 5909–5917. https://doi.org/10.1002/2015GL064236

Rignot, E., Fenty, I., Xu, Y., Cai, C., Velicogna, I., Cofaigh, C. Ó., et al. (2016). Bathymetry data reveal glaciers vulnerable to ice-ocean interaction in Uummannaq and Vaigat glacial fjords, west Greenland. *Geophysical Research Letters*, *43*, 2667–2674. https://doi.org/10.1002/2016GL067832

Schellenberger, T., Dunse, T., Kaab, A., Kohler, J., & Reijmer, C. H. (2015). Surface speed and frontal ablation of Kronebreen and Kongsbreen, NW Svalbard, from SAR offset tracking. *The Cryosphere*, *9*(6), 2339–2355. https://doi.org/10.5194/tc-9-2339-2015

Schild, K. M., & Hamilton, G. S. (2013). Seasonal variations of outlet glacier terminus position in Greenland. *Journal of Glaciology*, *59*(216), 759–770. https://doi.org/10.3189/2013JoG12J238

Schwanghart, W., & Kuhn, N. J. (2010). TopoToolbox: A set of Matlab functions for topographic analysis. *Environmental Modelling & Software*, *25*(6), 770–781. https://doi.org/10.1016/j.envsoft.2009.12.002

Sciascia, R., Straneo, F., Cenedese, C., & Heimbach, P. (2013). Seasonal variability of submarine melt rate and circulation in an east Greenland fjord. *Journal of Geophysical Research: Oceans*, *118*, 2492–2506. https://doi.org/10.1002/jgrc.20142

Seale, A., Christoffersen, P., Mugford, R. I., & O'leary, M. (2011). Ocean forcing of the Greenland ice sheet: Calving fronts and patterns of retreat identified by automatic satellite monitoring of eastern outlet glaciers. *Journal of Geophysical Research*, *116*, F03013. https://doi.org/10.1029/2010JF001847

Slater, D. A., Goldberg, D. N., Nienow, P. W., & Cowton, T. R. (2016). Scalings for submarine melting at tidewater glaciers from buoyant plume theory. *Journal of Physical Oceanography*, *46*(6), 1839–1855. https://doi.org/10.1175/JPO-D-15-0132.1

Slater, D. A., Nienow, P. W., Cowton, T. R., Goldberg, D. N., & Sole, A. J. (2015). Effect of near-terminus subglacial hydrology on tidewater glacier submarine melt rates. *Geophysical Research Letters*, *42*, 2861–2868. https://doi.org/10.1002/2014GL062494

Slater, D. A., Nienow, P. W., Goldberg, D. N., Cowton, T. R., & Sole, A. J. (2017). A model for tidewater glacier undercutting by submarine melting. *Geophysical Research Letters*, *44*, 2360–2368. https://doi.org/10.1002/2016GL072374

Smith, S. D. (1993). Hindcasting iceberg drift using current profiles and winds. *Cold Regions Science and Technology*, *22*(1), 33–45. https://doi.org/10.1016/0165-232X(93)90044-9

Sole, A. J., Mair, D. W. F., Nienow, P. W., Bartholomew, I. D., King, M. A., Burke, M. J., & Joughin, I. (2011). Seasonal speedup of a Greenland marine-terminating outlet glacier forced by surface melt-induced changes in subglacial hydrology. *Journal of Geophysical Research*, *116*, F03014. https://doi.org/10.1029/2010JF001948

Stevens, L. A., Straneo, F., Das, S. B., Plueddemann, A. J., Kukulya, A. L., & Morlighem, M. (2016). Linking glacially modified waters to catchment-scale subglacial discharge using autonomous underwater vehicle observations. *The Cryosphere*, *10*(1), 417–432. https://doi.org/10.5194/tc-10-417-2016

Straneo, F., Curry, R. G., Sutherland, D. A., Hamilton, G. S., Cenedese, C., Vage, K., & Stearns, L. A. (2011). Impact of fjord dynamics and glacial runoff on the circulation near Helheim Glacier. *Nature Geoscience*, *4*(5), 322–327. https://doi.org/10.1038/ngeo1109

Straneo, F., Hamilton, G. S., Sutherland, D. A., Stearns, L. A., Davidson, F., Hammill, M. O., et al. (2010). Rapid circulation of warm subtropical waters in a major glacial fjord in east Greenland. *Nature Geoscience*, *3*(3), 182–186. https://doi.org/10.1038/ngeo764

Straneo, F., & Heimbach, P. (2013). North Atlantic warming and the retreat of Greenland's outlet glaciers. *Nature*, *504*(7478), 36–43. https://doi.org/10.1038/nature12854

Sutherland, D. A., & Straneo, F. (2012). Estimating ocean heat transports and submarine melt rates in Sermilik Fjord, Greenland, using lowered acoustic Doppler current profiler (LADCP) velocity profiles. *Annals of Glaciology*, *53*(60), 50–58. https://doi.org/10.3189/2012AoG60A050

Svendsen, H., Beszczynska-Møller, A., Hagen, J. O., Lefauconnier, B., Tverberg, V., Gerland, S., et al. (2002). The physical environment of Kongsfjorden-Krossfjorden, an Arctic fjord system in Svalbard. *Polar Research*, *21*(1), 133–166. https://doi.org/10.1111/J.1751-8369.2002.Tb00072.X

Truffer, M., & Motyka, R. J. (2016). Where glaciers meet water: Subaqueous melt and its relevance to glaciers in various settings. *Reviews of Geophysics*, *54*, 220–239. https://doi.org/10.1002/2015RG000494

van den Broeke, M., Bamber, J., Ettema, J., Rignot, E., Schrama, E., van de Berg, W. J., et al. (2009). Partitioning recent Greenland mass loss. *Science*, *326*(5955), 984–986. https://doi.org/10.1126/science.1178176

Van Pelt, W., & Kohler, J. (2015). Modelling the long-term mass balance and firn evolution of glaciers around Kongsfjorden, Svalbard. *Journal of Glaciology*, *61*(228), 731–744. https://doi.org/10.3189/2015JoG14J223

Vieli, A., & Nick, F. M. (2011). Understanding and modelling rapid dynamic changes of tidewater outlet glaciers: Issues and implications. *Surveys in Geophysics*, *32*(4–5), 437–458. https://doi.org/10.1007/S10712-011-9132-4

Wagner, T. J. W., Dell, R. W., & Eisenman, I. (2017). An analytical model of iceberg drift. *Journal of Physical Oceanography*, *47*(7), 1605–1616. https://doi.org/10.1175/jpo-d-16-0262.1

Xu, Y., Rignot, E., Menemenlis, D., & Koppes, M. (2012). Numerical experiments on subaqueous melting of Greenland tidewater glaciers in response to ocean warming and enhanced subglacial discharge. *Annals of Glaciology*, *53*(60), 229–234. https://doi.org/10.3189/2012aog60a139